ChemCatChem

Research Article
doi.org/10.1002/cctc.202501270

Chemistry Europe
European Chemical Societies Publishing

www.chemcatchem.org

Catalytic Activity of Cobalt Ferrites in Water Oxidation Reactions and Its Defect Dependency

Anna Rabe,[a] Ahmed Gamal Attallah,[b, c] Benedikt Eggert,[a] Eric Hirschmann,[b] Soma Salamon,[a] Joachim Landers,[a] Lea Kämmerer,[a] Nicolas Cosanne,[d] Adarsh Koul,[e] Eko Budiyanto,[f] Wolfgang Schuhmann,[e] Malte Behrens,[d] and Heiko Wende*[a]

$CoFe_2O_4$ (CFO) nanoparticles were synthesized via controlled co-precipitation with subsequent calcination at 400 °C, 500 °C, and 600 °C to systematically investigate the influence of thermal treatment on mesostructure, catalytic performance, and especially defect landscape. Structural characterization revealed enhanced crystallinity, sintering, and reduced defect concentration with increasing calcination temperature. Mössbauer spectroscopy and magnetometry indicated increased inversion parameters, improved magnetic alignment, and reduced spin canting, which is consistent with enhanced atomic diffusion during calcination and structural ordering. Positron annihilation lifetime spectroscopy confirmed a calcination-dependent decrease in vacancy-type defects. Catalytic testing showed diverging trends: chemical water oxidation (CAN test) activity increased with calcination temperature, but electrochemical oxygen evolution (OER) activity decreased. The opposing behavior is attributed to distinct differences in mechanism: CAN test reactivity is dominated by surface site availability, whereas OER benefits from defect mediated conductivity and charge-transfer. These results underline the pivotal role of defect engineering while tailing spinel catalysts and highlight that optimal mesostructures depend strongly on the target reaction.

1. Introduction

Water splitting is a cornerstone reaction in the pursuit of sustainable hydrogen production, offering a clean and renewable pathway to meet the ever growing global energy demand.[1] Central to the viability of this process is the development of efficient and stable catalysts, particular for the electrochemical oxygen evolution reaction (OER), which is kinetically sluggish and therefore leads to high overpotentials.[2] Among the various classes of investigated materials, transition metal oxides, especially spinel-type oxides such as cobalt ferrite, pure cobalt spinel and doped analogues, have emerged as promising candidates due to being earth abundant, intrinsic structural stability and the presence of redox-active cations.[3–7]

However, the catalytic performance of these materials is highly sensitive to their composition and mesostructure, meaning crystallinity, cation distribution, pore size, and the concentration and type of defects.[8–10] These mesostructural features not only influence surface reactivity, but also more bulk-like properties such as charge transport and ion mobility, which are both crucial factors, especially for electrochemical water oxidation.[11] Defects such as oxygen vacancies, cation vacancies, and dislocation play particularly critical roles, also their specific functions differ depending on the reaction environment.[12] While chemical water oxidation with a sacrificial single-electron oxidant is largely governed by the nature and availability of surface-active sites,[13,14] electrochemical processes introduce additional complexity through requirement of, e.g., active phase formation, electronic conductivity and efficient charge transfer kinetics.[11,15–17]

Understanding and controlling the mesostructure, including defect landscapes, is thus essential of the knowledge-based design of high-performance catalysts. These characteristics can be finely and reproducibly tuned through highly controlled synthesis parameters during precursor synthesis and particularly thermal treatment conditions such as calcination temperature. In this study, we systematically investigate the influence of calcination temperature on the mesostructure and catalytic activity of cobalt ferrite, with a special emphasis on correlating defect structures with observed reactivity trends.

[a] Dr. A. Rabe, Dr. B. Eggert, Dr. S. Salamon, Dr. J. Landers, Dr. L. Kämmerer, Prof. Dr. H. Wende
Faculty of Physics and Center for Nanointegration Duisburg-Essen (CENIDE), University of Duisburg-Essen, Duisburg, Germany
E-mail: heiko.wende@uni-due.de

[b] Dr. A. G. Attallah, Dr. E. Hirschmann
Institute of Radiation Physics, Helmholtz-Zentrum Dresden-Rossendorf, Dresden 01328, Germany

[c] Dr. A. G. Attallah
Physics Department, Faculty of Science, Minia University, Minia 61519, Egypt

[d] N. Cosanne, Prof. Dr. M. Behrens
Institute for Inorganic Chemistry, Christian-Albrechts-Universität zu Kiel, Kiel 24148, Germany

[e] Dr. A. Koul, Prof. Dr. W. Schuhmann
Analytical Chemistry – Center for Electrochemical Sciences (CES), Faculty of Chemistry and Biochemistry, Ruhr University Bochum, Bochum 44780, Germany

[f] Dr. E. Budiyanto
Max-Planck Institute für Kohlenforschung, Mülheim an der Ruhr 45470, Germany

To achieve this, next to typical characterization techniques such as PXRD, SEM, Mössbauer spectroscopy, magnetometry, and BET analysis, we employ positron annihilation lifetime spectroscopy (PALS), an advanced characterization technique capable of providing detailed insights into the type, concentration, and evolution of vacancy-type defects within the catalysts. By comparing catalytic behavior across different reactions, namely chemical and electrochemical water oxidation, we aim to disentangle structure-reactivity relationships that govern performance. Ultimately, this work provides a deeper understanding of how mesostructural features, particularly defects, impacts catalytic activity, paving the way for knowledge-based catalyst design.

We structured the paper as follows: First, we present the synthesis of the catalysts, then we turn to structural characterization, including analysis of magnetic properties and defect characterization. In the second part, we investigate the different trends observed in chemical and electrochemical water oxidation and correlate them with the structural and magnetic characterizations.

2. Results and Discussion

2.1. Synthesis and Characterization

For synthesis of the systematic calcination series investigated in this work, a cobalt ferrite precursor was directly co-precipitated under highly controlled conditions in an automated lab reactor system, similar to that reported in Rabe et al.[8] Subsequently, the precursor was calcined at three different temperatures, namely 400 °C, 500 °C, and 600 °C. The three $CoFe_2O_4$ samples are labelled according to their final calcination temperature CFO400, CFO500, and CFO600.

As already reported,[8] the precursor was thermally treated, to trigger the crystallization of potential X-ray amorphous by-phases. In this paper, thermal treatment does not only serve this purpose, but the different calcination temperatures are assumed to result in different degrees of domain and particle size, crystallinity, and defect density. Especially the effect of the defect landscape is characterized using positron lifetime annihilation spectroscopy and is correlated with the catalytic activity.

Thermogravimetric analysis (TGA) of the as-prepared sample is shown in Figure 1, left. Even though in X-ray powder diffraction (PXRD) only a cobalt ferrite diffraction pattern and no additional reflections from potential by-phases were observed, a significant weight loss was detected at temperatures below 300 °C, which is assigned to drying and decomposition of potential amorphous hydroxide or carbonate precursor phases. After calcination at only 400 °C, no pronounced weight loss is observed anymore, and any potential amorphous by-phases are assumed to have crystallized.

Elemental analysis was performed for all samples and showed the desired cobalt to iron ration of 1:2. Additionally, after calcination at 300 °C a minor amount of hydrogen was detected, agreeing with the weight loss below 300 °C observed in TGA. Together with the minor mass loss in TGA at this temperature, only the samples at or above 400 °C calcination temperature were considered phase pure. The PXRD reflections become sharper with increasing calcination temperature, indicating a higher degree of crystallinity. The surface area was analyzed using nitrogen physisorption and was 80 m^2/g for CFO 400, 42 m^2/g for CFO500 and 15 m^2/g for CFO 600. Figure 2 shows scanning electron microscopy (SEM) micrographs of the three calcined samples. With increasing calcination temperature, larger particles due to sintering are observed, agreeing with the increasing crystallinity and particle growth indicated by sharper PXRD reflections and the decrease in surface area from the Brunauer–Emmett–Teller (BET) technique. The N_2 physisorption adsorption-desorption isotherms are further analyzed to examine the pore structures of the cobalt ferrite calcination series samples (Figure 3). These adsorption–desorption isotherms exhibit type H1 hysteresis loops for all cobalt ferrite samples in the calcination series, indicating the adsorption-desorption behavior of mesopores formed between agglomerated particles.[19] This result agrees well with the morphology observed in the SEM micrographs (Figure 2), which reveals the mesoporous texture between the agglomerated particles.

To study changes in magnetic structure and site-occupation connected to structural modifications during the annealing process, we performed Mössbauer spectroscopy at 4.3 K in an external magnetic field of 5 T (Figure 4). We observe two sextet subspectra corresponding to Fe^{3+} on the tetrahedral A-sites (green) and octahedral B-sites (blue), reproduced here via narrow hyperfine field distributions. The subspectra show partial splitting due to the sublattices' antiparallel alignment, allowing for the resolution of both contributions and the determination of relative subspectral intensities reflecting the Fe site occupation in the three samples, usually described in spinels via the inversion parameter x shown in Table 1. This approach reveals an increase from $x_{CFO400} = 0.64(6)$ to $x_{CFO500} = 0.74(4)$ and $x_{CFO600} = 0.76(2)$ upon rising annealing temperature, toward the partially ordered inverse spinel structure most commonly present in $CoFe_2O_4$.[20,21] Due to the stronger overlap of spectral contributions at lower temperatures, the error margin is comparatively higher. Still, we register a first strong increase in inversion parameter when going to 500 °C, visible already to the naked eye in the corresponding spectra by the change in amplitude of the first and last sextet lines of A- and B-site contribution, respectively. This could indicate an onset of a necessary level of atomic diffusion to allow this considerable change in Fe ion distribution to take place at this temperature, with a minor, further increase upon going to even higher annealing temperatures.

At the same time, the degree of magnetic alignment, which is expected to show a correlation to the presence of structural defects, can be analyzed based on the relative intensity A_{23} of absorption lines 2 and 3, providing the average angle between spin and γ-ray incidence direction (here being parallel to the magnetic field), also known as spin canting angle. Here, we observe higher average canting angles for octahedral lat-

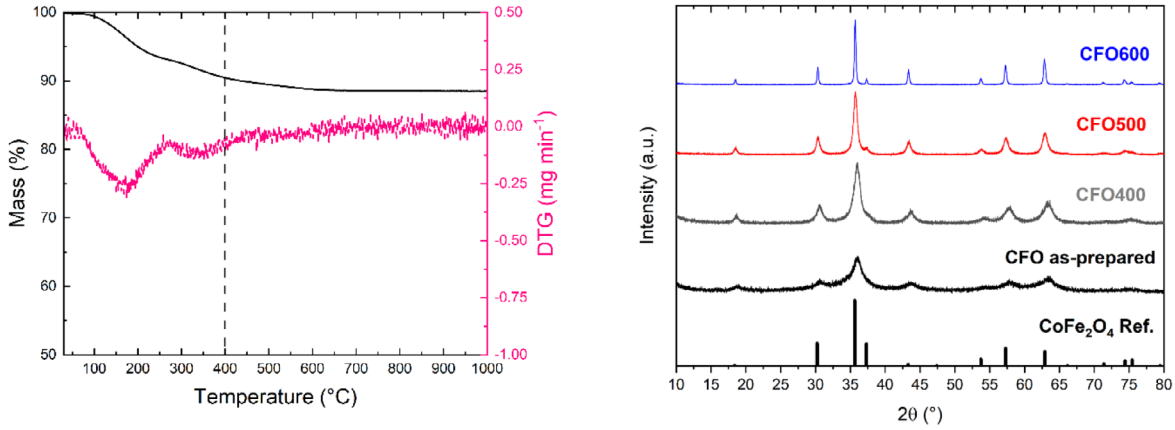

Figure 1. Left: Thermogravimetric analysis of the as-prepared $CoFe_2O_4$. Right: PXRD patterns of the as-prepared cobalt ferrite and after calcination at the different temperatures. $CoFe_2O_4$ reference from Ref. [18].

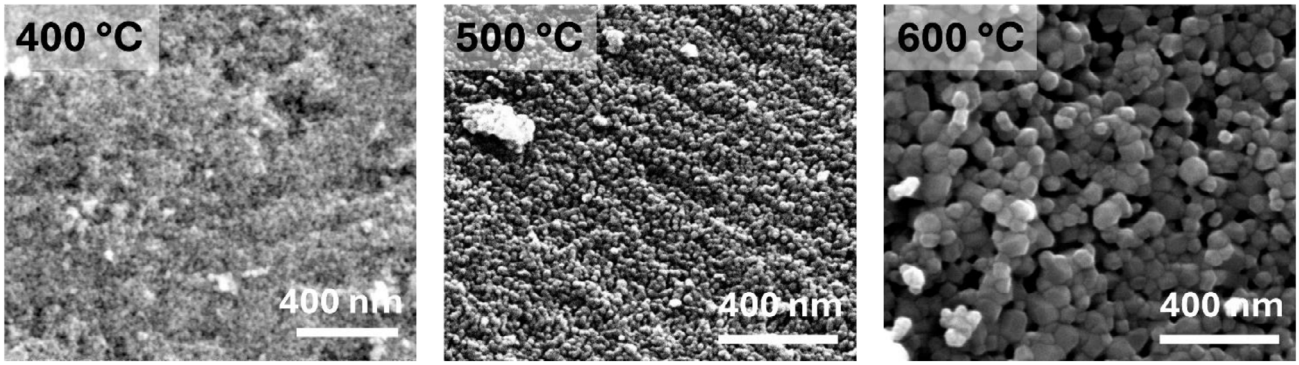

Figure 2. SEM images of the cobalt ferrite calcination series.

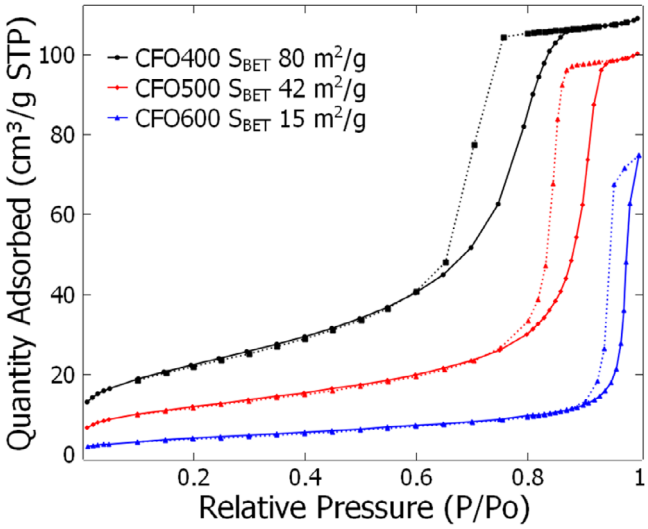

Figure 3. N_2 physisorption adsorption-desorption isotherms of the cobalt ferrite calcination series. Solid lines indicate adsorption branches and dotted lines indicate desorption branches.

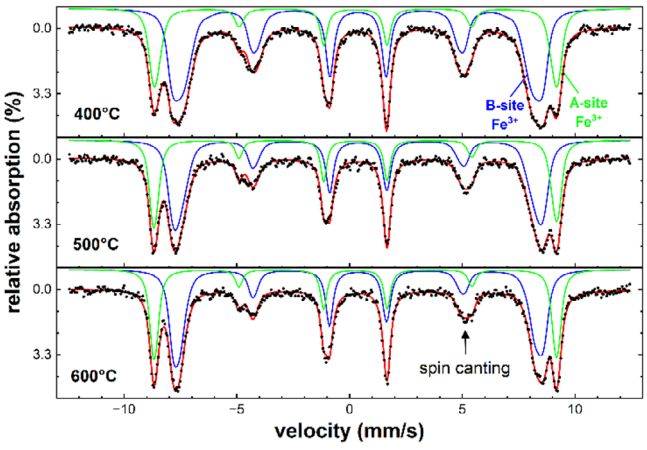

Figure 4. Mössbauer spectroscopy of samples annealed at 400 °C, 500 °C, and 600 °C, recorded at 4.3 K in an external magnetic field of 5 T parallel to the γ-ray incidence direction.

tice positions, which is a known phenomenon in most spinel systems.[22] In addition, a decrease in canting angle is detected –, i.e., an increasing degree of magnetic alignment – for higher annealing temperature, likely being connected to the combination of improved lattice structure and rising particle size, leading to a lower number of Fe surface positions.

M(H) loops up to a maximum field of ± 9 T were recorded for samples of all calcination temperatures at both 4.3 K and 300 K to determine the overall magnetic character, as well as the saturation behaviour at high fields (Figure 5). Generally speaking, all measurements show a consistent rise of the magnetization

Table 1. Inversion parameter x and average spin canting angles of A- and B-site Fe^{3+} for sample material annealed at calcination temperatures of 400 °C to 600 °C.

Calcination temperature	Inversion parameter	Θ_A (°)	Θ_B (°)
400 °C	0.64(6)	30(1)	38(1)
500 °C	0.74(4)	28(1)	33(1)
600 °C	0.76(2)	27(1)	31(1)

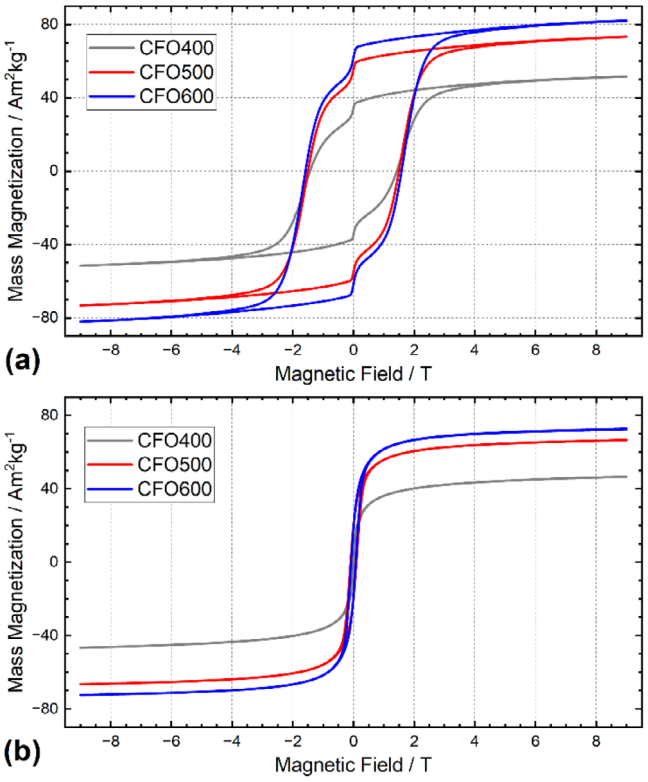

Figure 5. M(H) curves recorded up to magnetic fields of ±9 T recorded at 4.3 K (a) and 300 K (b).

upon increasing calcination temperature, valid in both the low-field range as well as the high-field regions of the M(H) loops, except for a slightly stronger curvature of M(H) for material calcinated at 400 °C indicating a somewhat slower approach to saturation, matching higher canting angles discussed in the Mössbauer spectroscopy section above. A comparison of the individual graphs of each set shows strong consistency in terms of hysteresis shape and saturation behavior, with only minute differences visible in coercivity observed at 300 K. All measurements display a minor soft-magnetic contribution upon going through zero field, which was associated in the literature, e.g., with reorientation of surface spins.[23]

This increase in magnetization is consistent with the improving magnetic alignment visible in Mössbauer spectra recorded at 5 T. Naturally, marked changes in magnetization of spinel systems can also take place by variations in the inversion parameter as observed upon calcination at 500 °C, however, for $CoFe_2O_4$, a redistribution of low magnetic moment Co^{2+} preferably to the B-site will usually result in a decrease of saturation magnetization M_S. Therefore, we would rather assign the rise in M_S noticeable here to the improved magnetic ordering than to a redistribution of Co and Fe ions.

Next to the thorough mesostructural characterization of the as-prepared and all calcined cobalt ferrite samples, positron annihilation lifetime spectroscopy (PALS) was performed to learn more about the defect structure of the thermally treated samples and consequently to better understand their catalytic activity.

Table 2 shows the two short-lived positron lifetimes τ_1 and τ_2, the average lifetime and the corresponding intensities for CFO400, CFO500, and CFO600. The presence of only two components suggests that a single defect type dominates the annihilation environment. In this framework, τ_2 is attributed to vacancy-type defects, and τ_1 is commonly interpreted as a reduced bulk lifetime. This reduction occurs because a significant fraction of positrons is trapped at vacancy sites, which lowers the contribution from bulk-like annihilation. Consequently, τ_1 becomes shorter than the actual bulk lifetime. Based on this, the Simple Trapping Model (STM) can be applied to estimate the true bulk lifetime using the measured values of τ_1, τ_2, and their intensities.[24,25]

For $CoFe_2O_4$ (CFO), the expected bulk lifetime is ~199 ps.[26] However, STM analysis of our CFO samples yielded recalculated values between 270 and 300 ps - significantly higher than the literature value. Attempts to include an additional lifetime component in the analysis were inconclusive, indicating the presence of an additional, unresolved defect. This points toward the presence of a secondary defect type that overlaps with the reduced lifetime, thereby driving τ_1 to higher values. The nature of this defect type cannot be clearly identified. Presumably, these non-resolvable defects can be extended defects like dislocations not containing monovacancies.[27] Dislocations are known to produce positron lifetimes slightly longer than the bulk but these are not easily distinguishable as separate components in the spectrum.[28] In this case, τ_1 is a weighted average of two contributions: a reduced bulk lifetime and, likely, dislocations. At lower calcination temperatures, the contribution from dislocations is minor, and τ_1 mainly reflects a reduced bulk lifetime. As calcination temperature increases, dislocations become more prominent, gradually shifting τ_1 toward values near the expected bulk lifetime.[29] However, this apparent convergence should not be interpreted as a signature of a defect-free bulk system. The persistent presence of τ_2 confirms that vacancy-type defects remain. The increase in τ_1 intensity (I_1) with temperature further supports the growing role of dislocations, which have a higher trapping cross-section.

The second component τ_2 is attributed to larger vacancy clusters, likely located at grain boundaries, and exhibits almost no change with calcination temperature (~ constant cluster size) with their concentration (I_2) decreasing with increasing calcination temperature. This can be connected to the higher diffusion deduced from inversion parameters from Mössbauer spectroscopy, as shown above. The qualitative trend summarized in Table 2 reflects a temperature-dependent defect evolution. The average positron lifetime, calculated as $\tau_{avg} = \tau_1 I_1 + \tau_2 I_2$, serves as a cumulative indicator of the material's defect content. An average positron lifetime exceeding that of defect-free

Table 2. PALS-derived lifetime components and intensities of CFO samples calcined at different temperatures. The average lifetime $\tau_{avg.} = \tau_1 \times I_1 + \tau_2 \times I_2$ is also presented.

Calcination T (°C)	τ_1 (ns)/I_1 (%)	τ_2 (ns)/I_2 (%)	$\tau_{avg.}$ (ns)
400	0.185 ± 0.004/20.06 ± 0.89	0.36 ± 0.001/79.63 ± 0.89	0.323 ± 0.007
500	0.190 ± 0.003/27.02 ± 1.06	0.355 ± 0.001/72.71 ± 1.05	0.309 ± 0.008
600	0.204 ± 0.005/41.29 ± 2.12	0.360 ± 0.004/52.40 ± 2.39	0.272 ± 0.018

bulk material signifies the presence of open-volume defects,[30] and correlates with defect type and density.[31] The $\tau_{avg.}$, overall defect concentration, is decreasing with calcination temperature, indicating defect healing. This agrees strongly with the sharpening of the reflections in PXRD, indicating higher crystallinity. Also, the sintering made visible through SEM investigations and the decreasing surface area detected by BET analysis confirm the hypothesis of defect healing with increasing temperature.

2.2. Catalytic Performance

After thorough characterization of the mesostructure, the three calcined cobalt ferrites samples were tested for their activity in chemical water splitting, using Ce^{4+} in the form of ceric ammonium nitrate (CAN) as an oxidizing agent and electrochemical oxygen evolution reaction (OER) in alkaline condition. CAN is an oxidant for chemical OER catalysis known in the literature and can be used to predict activity in electrochemical OER.[32,33] Due to the stability of CAN in solution,[32] the observed oxygen stems from the catalytic activity of the catalyst. However, it can only be tested in acidic conditions due to the pH of CAN,[32] in contrast to the electrochemical tests, which are performed under alkaline conditions. In this study, the initial rate of the CAN test was used to compare the activity of the cobalt ferrites. For the electrochemical OER activity current densities at 1.85 V versus RHE were extracted (Figure 6).[3] A detailed description of the performed measurements can be found in the experimental part of this paper.

The initial rates for the CAN test increased with increasing calcination temperature. The initial rate for the sample calcined at 500 °C was already subject of a former publication.[8] Within the determined error bars, the initial rates are the same, proving reproducibility of the synthesis. For the alkaline oxygen evolution reaction, the current densities decreased with increasing calcination temperature, which represents a decrease in activity.

These inverse trends for the oxidation reactions may be explained in part by the difference in acidity, but the different driving forces of the reactions are also to be considered. The driving force is purely chemical and governed by the uniform exposure of the catalyst's surface to the oxidation potential of the dissolved Ce^{4+} ions,[8,13] which serve as single electron transfer agents. The water oxidation reaction requires four redox equivalents and can be maintained by continuous supply of four fresh Ce^{4+} cations to the reaction site from the reaction fluid with only little relevance of transport phenomena in the solid catalyst. Interestingly, even though the surface area of the

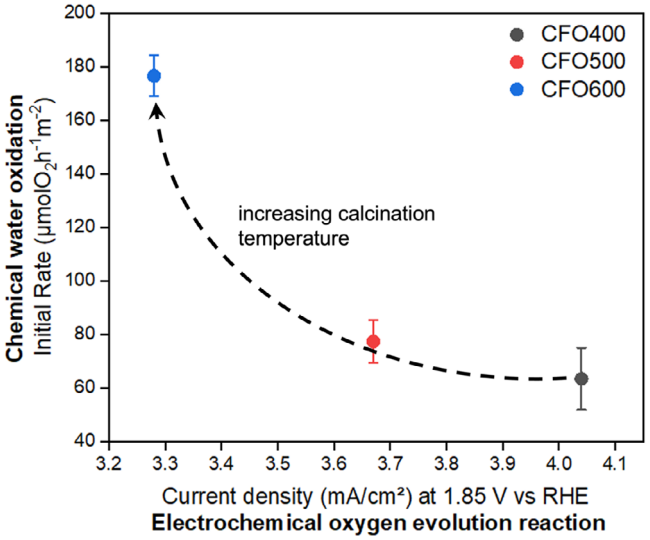

Figure 6. Initial rates for chemical water oxidation versus current densities at 1.85 V versus RHE for electrochemical OER for the calcination series. The dashed line is presented to guide the eye to show the trend with increasing calcination temperature.

cobalt ferrite decreases with increasing calcination temperature, the catalytic activity normalized to the surface area increases. This counterintuitive trend can be attributed to the improved structural and electronic properties of the catalysts induced by treatment at higher temperatures. As shown by PXRD and Mössbauer spectroscopy, higher calcination temperatures lead to enhanced crystallinity and an increased degree of inversion, which indicates a higher fraction of Co^{2+} occupying octahedral lattice sites within the spinel. A $Co^{2+} \rightarrow Co^{3+}$ transition is likely involved in the formation of the active site for water oxidation under the relevant redox potentials.[8] This transition should be facilitated for Co^{2+} at octahedral sites due to the higher ligand field stabilization energy for the expected d^6 low spin configuration. This easier in situ formation of active Co^{3+} species at the surface is assumed to lead to a better redox activity and therefore higher rates in the oxygen evolution process for more inverse spinels. Furthermore, the higher degree of structuring is assumed to lead to a higher intrinsic activity for chemical oxygen evolution for the samples with higher calcination temperature.

For the electrochemical OER on the other hand, the activity can be affected by a lot of parameters and is not limited to the exposed active surface area. Here, transport phenomena in the solid such as conductivity, but also binder effects etc. play a major role. The observed decrease in activity in electrochemical OER with increasing calcination temperature can

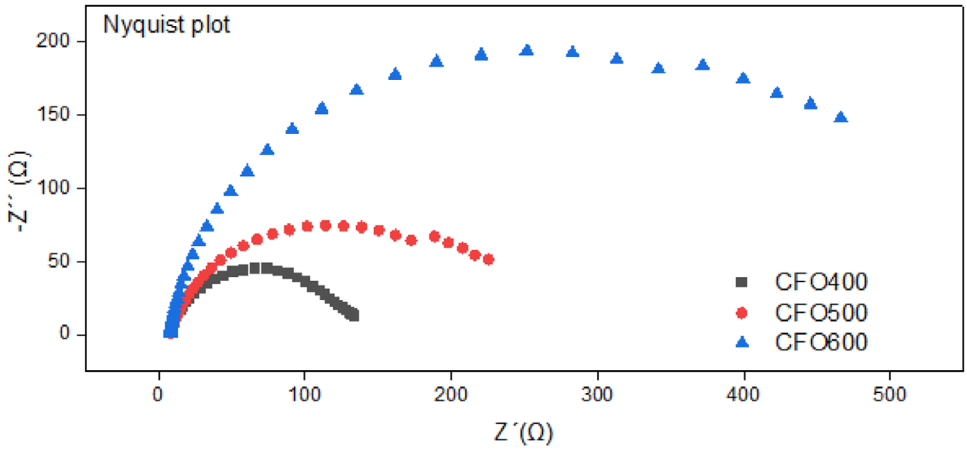

Figure 7. Nyquist plot of the three catalysts performed at 1.9 V versus RHE at a rotation rate of 1600 rpm.

be strongly correlated with the concurrent reduction in defect concentration detected by PALS. As the particles become more crystalline at higher temperatures, both bulk and surface defects are significantly reduced. While this enhanced structural ordering was beneficial in chemical water oxidation with its different prerequisites for activity, in electrochemistry it is detrimental. One explanation might be the hindered formation of the active phase. It is well-known that in OER, the as-prepared catalyst only functions as a precursor and for cobalt-containing oxides, an amorphous or oxy-hydroxide like phase containing Co^{3+} centers is formed as a shell on the surface of the catalyst at anodic potentials.[15–17,34] For its formation, connectivity through the solid to the back contact of the electrode and related transport phenomena are required unlike the CAN test, where the oxidizing potential is exerted by the fluid to the outer surface only. Also, a lower number of defects might negatively impact the electronic conductivity of the material. In spinel oxides like cobalt ferrites, charge transport is by electron hopping can be facilitated by defects and vacancies.[35,36] To analyze the charge transfer resistance of the catalysts, electrochemical impedance spectroscopy (EIS) measurements were performed at 1.9 V versus RHE, and the corresponding Nyquist plots are shown in Figure 7. The charge transfer resistance was found to increase systematically from C4 (≈120 Ω) to C5 (≈250 Ω) to C6 (≈500 Ω). This trend correlates with the overpotentials observed, i.e., higher charge transfer resistance is associated with higher overpotentials, highlighting the detrimental impact of sluggish charge transfer kinetics on the overall electrocatalytic performance.

An increased calcination temperature suppresses these transport pathways, resulting in poorer electronic conductivity and higher charge-transfer resistance at the electrode-electrolyte interface. Additionally, it can be assumed that adsorption of intermediates and the nucleation of the oxyhydroxide phase also take place at defective surface structures, further underlining the importance of the mesostructure of the active phase. All in all, these effects explain the observed decline in OER activity.

3. Conclusion

In this paper, a systematic series of cobalt ferrite samples was synthesized utilizing controlled co-precipitation with subsequent calcination at three temperatures, namely 400 °C, 500 °C, and 600 °C. The impact of thermal treatment on structural, magnetic, and catalytic properties was investigated. Comprehensive characterization revealed that increasing calcination temperature leads to enhanced crystallinity, particle growth, and a reduction in defect concentration. PXRD, BET, SEM, and TGA data all point toward significant structural ordering accompanied by sintering at higher calcination temperatures.

Mössbauer spectroscopy showed an increase in the inversion parameter and improved magnetic alignment with calcination temperature, attributed to enhanced atomic diffusion and reduced structural disorder. Magnetic measurements confirmed these trends, indicating higher magnetization and lower spin canting at elevated calcination temperatures. PALS data further supported the defect healing hypothesis by demonstrating a temperature dependent reduction in defect concentration such as vacancy clusters.

Catalytic testing showed a contrasting trend in activity depending on the reaction. Chemical water oxidation (CAN test) performance increased with calcination temperature, whereas electrochemical OER activity decreased. The increasing activity for CAN test can be explained by the different pathway compared to electrochemical water oxidation. In electrochemistry, defects can lead to higher conductivity and more complex electron and ion transport mechanisms play a role. For chemical water oxidation, only the surface is assumed to be involved in the reaction.

Overall, this work highlights the critical role of defect analysis, when trying to understand the reactivity of catalysts. Clearly, different reactions have different needs for the catalyst to perform best, but understanding the connection between mesostructure and activity is pivotal.

4. Experimental Section

4.1. Synthesis

The synthesis based on a previously published procedure was conducted in an automatic lab reactor system (*OptiMax 1001, Mettler Toledo*).[8] The $CoFe_2O_4$ precursor was co-precipitated by dosing 125 g of metal salt solution containing 0.233 M $Co(NO_3)_2x9H_2O$ and 0.566 M $Fe(NO_3)_3x6H_2O$ over the course of 1 h into the reactor, which was prefilled with 200 mL of distilled water. The pH was controlled by an InLab Semi-Micro-L pH electrode. To ensure a constant pH of 10, a 1.5 M NaOH solution was dosed automatically into the reactor. After co-precipitation, the material was aged at 10 °C for 1 h. During reaction and aging, the reactor was constantly purged with N_2 and stirred at 350 rpm. The precipitated $CoFe_2O_4$ was washed with water several times and dried in static air at 80 °C. Subsequently, 1 g of powder each was calcined at 400 °C, 500 °C, and 600 °C for 3 h in a muffle furnace.

4.2. Characterization

PXRD was performed with a Bruker D8 Advance diffractometer with a Cu X-ray source in Bragg Brentano geometry with a LynxEye XE-T detector. The samples were dispersed in ethanol on a PMMA sample holder and diffraction patterns were recorded in the angular range from 5° to 90° 2θ with a step size of 0.01° and a counting time of 1.5 s. During the measurements the sample holder was slowly rotated.

Scanning electron microscopy was conducted with an Aprea S LoVac (Thermo Fisher Scientific). Prior to measurement the samples were sputtered with Pt/Au.

The ratio of the incorporated metal cations was determined by atomic absorption spectroscopy (Thermo Electron Corporation, M-Series) of the as-prepared $Cofe_2O_4$. The carbon and hydrogen contents were determined by CNHS analysis. A twofold measurement was performed.

Thermogravimetric analysis of the directly co-precipitated $CoFe_2O_4$ precursor was carried out with a NETZSCH STA 449f F3 Jupiter (NETZSCH GmbH, Germany). The mass loss was recorded as a function of the temperature with a linear heating rate of β = 5 K min^{-1} in a temperature range from 30 °C to 1000 °C and a gas stream of O_2 (21 mL min^{-1} and Ar (79 mL min^{-1}).

BET surface areas were measured using N_2 physisorption at 77 K with a 3Flex Micromeritics instrument. Prior to measurements, the samples were degassed at 120 °C in vacuum for 4 h. The Brunauer–Emmett–Teller (BET) surface area was calculated within the 0.06–0.3 relative pressure range (P/P_0).

Mössbauer spectra were recorded in standard transmission geometry, using a ^{57}Co radiation source mounted on a WissEl driving unit operating in constant acceleration mode. A liquid helium bath cryostat was utilized to attain low temperatures and high fields, containing a superconducting solenoid in split pair geometry. A homogeneous magnetic field of 5 T was applied at the sample position, with the field orientation parallel to the γ-ray propagation direction (in-axis).

Magnetic properties were analyzed using the vibrating sample magnetometer (VSM) option of a Quantum Design PPMS DynaCool. The field dependent properties were characterized via M(H) loops recorded at 4.3 K and 300 K at magnetic fields up to 9 T.

Defect characterization was performed using positron annihilation lifetime spectroscopy (PALS). PALS measurements were carried out using a digitizer module (Acqiris DC 282) with 10-bit vertical resolution, coupled with three photomultiplier tubes (PMTs) equipped with Ce_2Br_3 scintillators supplied by Scionix Holland. Two of the detectors featured scintillators with dimensions Ø = 51 mm and h = 10 mm, while the third employed a thicker crystal (h = 25.4 mm), allowing for enhanced signal capture and suppression of backscattered photons. Signal processing and data collection were managed via a customized acquisition software,[37] enabling simultaneous detection across all channels. This setup allowed for the acquisition of up to six independent lifetime spectra per session, thus improving throughput and reducing overall measurement time. Powdered samples (~3 mm^3) were loaded into a dedicated holder together with a ^{22}Na positron source (20 µCi), which was encapsulated between 5 µm Kapton foils (DuPont de Nemours). The lifetime spectrum, represented by $N(t) = \Sigma\ [(I_i/\tau_i)\ \exp(-t/\tau_i)]$, was analyzed by fitting multi-exponential decay functions to the time-difference histograms. Here, τ_i and I_i denote the lifetime and relative intensity of the i-th annihilation channel, respectively, with $\Sigma I_i = 1$.[38,39]

Calibration and resolution estimation were performed using Fe, Al, and Sn reference materials with well-established lifetimes. The overall source contribution—comprising annihilation within the Kapton foils (0.382 ns, 10.4%) and the adhesive layer (2.60 ns, 0.2%)—amounted to approximately 10.6% of the total events. The time resolution function, determined during the fitting process, yielded an average full width at half maximum (FWHM) of 0.28 ns. The recorded spectra were analyzed with the PALSfit software[40] which identified two distinct sample-related lifetime components, τ_1 and τ_2, along with their intensities I_1 and I_2.

4.3. Catalysis

Chemical water oxidation was performed using Ce^{4+} as oxidizing agent. During the oxidation process of water to oxygen the single-electron oxidant Ce^{4+} is reduced to Ce^{3+} ($E^0(Ce^{3+}/\ Ce^{4+})$ = 1.72 V versus NHE at pH = 0)

$$4Ce^{4+} + 2H_2O \overset{CoFe_2O_4}{\rightarrow} 4H^+ + O_2 + 4Ce^{3+}$$

For determination of the initial rates for chemical water oxidation, 100 mg of catalyst were dispersed in 45 mL water. The setup was purged with Ar (50 mL min^{-1}) to ensure an oxygen free environment. 5 mL of a $(NH_4)_2Ce(NO_3)_6$ solution (2.5 mol L^{-1}) were added to the dispersion, and the evolving oxygen was detected by an oxygen analyzer (EC900, Systech Illinios) over 2 h. For each catalyst twofold measurements were performed.

Electrochemical experiments were performed using a three-electrode cell configuration connected to a Metrohm Autolab PGSTAT potentiostat equipped with a rotator (Metrohm). A double-junction Ag/AgCl reference electrode (Metrohm) was employed, containing 3 M KCl in the inner chamber and 1 M KOH in the outer chamber. A platinum mesh served as the counter electrode and was placed in a separate compartment isolated by a glass frit to prevent cross-contamination during measurements.

The working electrode was a glassy carbon rotating disk electrode (geometric area: 0.1134 cm^2), which was polished to a mirror-like finish using 0.05 µm alumina slurry prior to catalyst deposition. Catalyst ink was prepared by dispersing 1 mg of catalyst powder in 200 µL of a solvent mixture containing ultrapure water, ethanol, and Nafion solution in a 49:49:2 volume ratio. A 4.8 µL aliquot of this ink was drop-cast onto the polished glassy carbon surface, resulting in a catalyst loading of approximately 210 µg cm^{-2}. After drying, the modified electrode was used for all electrochemical tests.

All experiments were conducted in 1 M KOH electrolyte that had been purified using Chelex 100 chelating ion exchange resin (Bio-Rad) to eliminate trace metal contaminants. Prior to measurements, the electrolyte was purged throughout all electrochemical measurements to preserve inert conditions.

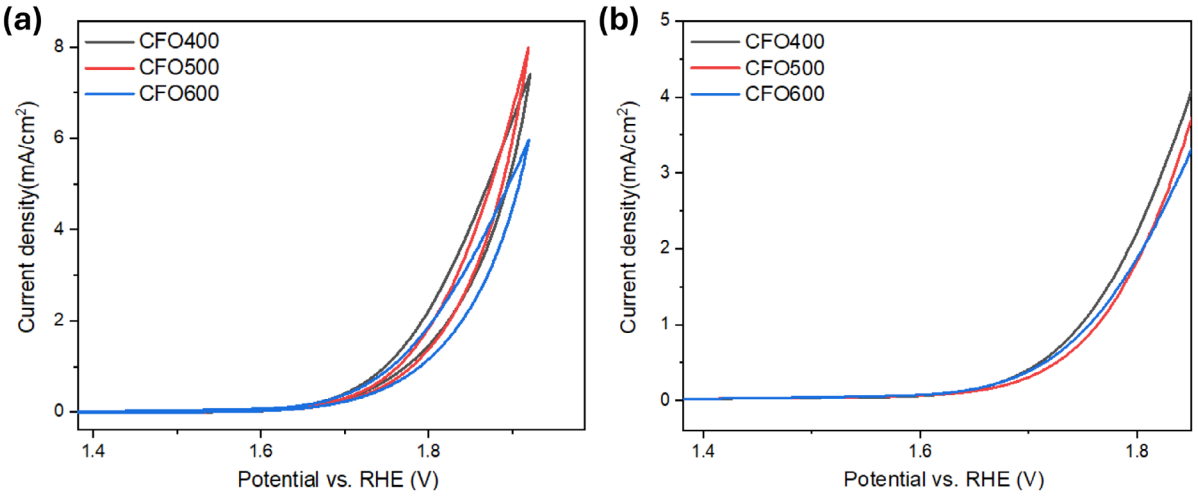

Figure 8. (a) CV for the 3 catalysts (averaged for 3 electrodes) performed at 5 mV/s scan rate and 1600 rpm rotation rate. (b) The same data of the CV shown only in the forward direction (LSV).

The open-circuit potential (OCP) was recorded for 100 s to stabilize the system. Electrochemical impedance spectroscopy (EIS) was then carried out at 0 V versus OCP over a frequency range from 100 kHz to 1 Hz to determine the uncompensated solution resistance (R_s).

Electrode conditioning was conducted using 20 consecutive cyclic voltammetry (CV) scans between 0.0 V and 0.3 V versus OCP at a scan rate of 100 mV/s.

Subsequent evaluation of oxygen evolution reaction (OER) activity was performed via linear sweep voltammetry (LSV) from 0.0 V to 0.9 V versus at 5 mV/s as shown in Figure 8b. During LSV, the electrode was rotated at 1600 rpm to enhance mass transport and ensure effective bubble removal from the surface.

All measured potentials were converted to the reversible hydrogen electrode (RHE) scale using the following equation:

$$E_{RHE} = E_{Ag/AgCl/3MKCl} + E^0_{Ag/AgCl/3MKCl} + 0.059 \times Ph$$

where $E_{Ag/AgCl/\ 3\ M\ KCl}$ is the potential measured versus an Ag/AgCl/3 M KCl reference electrode, and $E^0_{Ag/AgCl/3\ M\ KCl}$ is taken as 0.207 V at 25 °C. The pH was estimated using the following relation:

$$pH = 14 + \log(c(OH^-)) + \log(\gamma)$$

where γ represents the activity of water, assumed to be 0.766 based on literature values.[41] However, γ was not explicitly factored into the pH calculation. All potential conversions were made assuming ambient conditions (25 °C).

To account for solution resistance (iR) effects, measured potentials were further corrected using the following equation:

$$E_{RHE,corrected} = E_{RHE} - i \times R_u$$

where i is the instantaneous current from the voltammogram, and R_u is the uncompensated resistance obtained from EIS.

Acknowledgments

The research was funded by the Deutsche Forschungsgemeinschaft (DFG, German Research Foundation) in the framework of the Collaborative Research Center / Transregio "Heterogeneous Oxidation Catalysis in the Liquid Phase"- (Project number 388390466, Projects B02, C01, A02). Furthermore, the authors would like to thank Dr. Kateryna Loza (SEM), and Robin Meya (AAS) for their assistance in the experimental work.

Open access funding enabled and organized by Projekt DEAL.

Conflict of Interests

The authors declare no conflict of interest.

Data Availability Statement

The data that support the findings of this study are available from the corresponding author upon reasonable request.

Keywords: Cobalt ferrite · Co-precipitation · Defects · Oxygen evolution reaction · Positron annihilation lifetime spectroscopy

[1] J. O. Abe, A. Popoola, E. Ajenifuja, O. Popoola, *Int. J. Hydrogen Energy* **2019**, *44*, 15072–15086. https://doi.org/10.1016/j.ijhydene.2019.04.068.
[2] N.-T. Suen, S.-F. Hung, Q. Quan, N. Zhang, Y.-J. Xu, H. M. Chen, *Chem. Soc. Rev.* **2017**, *46*, 337–365. https://doi.org/10.1039/C6CS00328A.
[3] C. C. L. McCrory, S. H. Jung, J. C. Peters, T. F. Jaramillo, *J. Am. Chem. Soc.* **2013**, *135*, 16977–16987. https://doi.org/10.1021/ja407115p.
[4] Q. Zhao, Z. Yan, C. Chen, J. Chen, *Chem. Rev.* **2017**, *117*, 10121–10211. https://doi.org/10.1021/acs.chemrev.7b00051.
[5] S. Saddeler, U. Hagemann, S. Schulz, *Inorg. Chem.* **2020**, *59*, 10013–10024. https://doi.org/10.1021/acs.inorgchem.0c01180.
[6] S. Saddeler, G. Bendt, S. Salamon, F. T. Haase, J. Landers, J. Timoshenko, C. Rettenmaier, H. S. Jeon, A. Bergmann, H. Wende, *J. Mater. Chem. A* **2021**, *9*, 25381–25390.
[7] E. Budiyanto, M. Yu, M. Chen, S. DeBeer, O. Rüdiger, H. Tüysüz, *ACS Appl. Energy Mater.* **2020**, *3*, 8583–8594. https://doi.org/10.1021/acsaem.0c01201.
[8] A. Rabe, J. Büker, S. Salamon, A. Koul, U. Hagemann, J. Landers, K. Friedel Ortega, B. Peng, M. Muhler, H. Wende, *Chem. - Eur. J.* **2021**, *27*, 17038–17048. https://doi.org/10.1002/chem.202102400.
[9] A. Rabe, M. Jaugstetter, F. Hiege, N. Cosanne, K. F. Ortega, J. Linnemann, K. Tschulik, M. Behrens, *ChemSusChem* **2023**, *16*, e202202015.

[10] F. T. Haase, A. Rabe, F.-P. Schmidt, A. Herzog, H. S. Jeon, W. Frandsen, P. V. Narangoda, I. Spanos, K. Friedel Ortega, J. Timoshenko, *J. Am. Chem. Soc.* **2022**, *144*, 12007–12019. https://doi.org/10.1021/jacs.2c00850.
[11] J. Linnemann, K. Kanokkanchana, K. Tschulik, *ACS Catal.* **2021**, *11*, 5318–5346. https://doi.org/10.1021/acscatal.0c04118.
[12] T. Tatarchuk, *Nanomaterials* **2024**, *14*, 1640. https://doi.org/10.3390/nano14201640.
[13] J. Heese-Gartlein, D. M. Morales, A. Rabe, T. Bredow, W. Schuhmann, M. Behrens, *Chem.-Eur. J.* **2020**, *26*, 12256–12267. https://doi.org/10.1002/chem.201905090.
[14] C. E. Frey, P. Kurz, *Chem.-Eur. J.* **2015**, *21*, 14958–14968. https://doi.org/10.1002/chem.201501367.
[15] A. Bergmann, T. E. Jones, E. M. Moreno, D. Teschner, P. Chernev, M. Gliech, T. Reier, H. Dau, P. Strasser, *Nat. Catal.* **2018**, *1*, 711–719. https://doi.org/10.1038/s41929-018-0141-2.
[16] T. Wiegmann, I. Pacheco, F. Reikowski, J. Stettner, C. Qiu, M. Bouvier, M. Bertram, F. Faisal, O. Brummel, J. Libuda, J. Drnec, P. Allongue, F. Maroun, O. M. Magnussen, *ACS Catal.* **2022**, *12*, 3256–3268. https://doi.org/10.1021/acscatal.1c05169.
[17] F. Reikowski, F. Maroun, I. Pacheco, T. Wiegmann, P. Allongue, J. Stettner, O. M. Magnussen, *ACS Catal.* **2019**, *9*, 3811–3821. https://doi.org/10.1021/acscatal.8b04823.
[18] T. A. S. Ferreira, J. C. Waerenborgh, M. H. R. M. Mendonca, M. R. Nunes, F. M. Costa, *Solid State Sci.* **2003**, *5*, 383–392. https://doi.org/10.1016/S1293-2558(03)00011-6.
[19] K. S. W. Sing, D. H. Everett, R. A. W. Haul, L. Moscou, R. A. Pierotti, J. Rouquerol, T. Siemieniewska, *Pure Appl. Chem.* **1985**, *57*, 603-619. https://doi.org/10.1351/pac198557040603.
[20] M. R. De Guire, R. C. O'Handley, G. Kalonji, *J. Appl. Phys.* **1989**, *65*, 3167–3172. https://doi.org/10.1063/1.342667.
[21] S. Zerebecki, S. Salamon, J. Landers, Y. Yang, Y. Tong, E. Budiyanto, D. Waffel, M. Dreyer, S. Saddeler, T. Kox, *ChemCatChem* **2022**, *14*, e202101785.
[22] J. Marx, H. Huang, K. M. Salih, W. R. Thiel, V. Schünemann, *Hyperfine Interact.* **2016**, *237*, 41. https://doi.org/10.1007/s10751-016-1241-5.
[23] S. Xu, Y. Ma, G. Zheng, Z. Dai, *Nanoscale* **2015**, *7*, 6520–6526. https://doi.org/10.1039/C5NR00582E.
[24] R. N. West, *Adv. Phys.* **1973**, *22*, 263–383. https://doi.org/10.1080/00018737300101299.
[25] R. West, *Positrons in Solids*, Springer, Berlin, Heidelberg **1979**, pp. 89–144.
[26] K. B. Modi, N. H. Vasoya, V. K. Lakhani, T. K. Pathak, P. Nambissan, *Int. J. Spectrosc.* **2013**, *2013*, 1–11. https://doi.org/10.1155/2013/272846.
[27] J. Čížek, O. Melikhova, Z. Barnovská, I. Procházka, R. Islamgaliev, *J. Phys.: Conf. Ser.* **2013**, *443*, 012008, IOPPublishing.
[28] H. Häkkinen, S. Mäkinen, M. Manninen, *Europhys. Lett.* **1989**, *9*, 809–814. https://doi.org/10.1209/0295-5075/9/8/012.
[29] S. Assali, M. Elsayed, J. Nicolas, M. O. Liedke, A. Wagner, M. Butterling, R. Krause-Rehberg, O. Moutanabbir, *Appl. Phys. Lett.* **2019**, *114*, 251907. https://doi.org/10.1063/1.5108878.
[30] Z. Wu, D. Chaykina, H. Schreuders, H. Schut, M. De Boer, M. O. Liedke, M. Butterling, A. Wagner, M. Dickmann, E. Brück, *Phys. Rev. Mater.* **2025**, *9*, 015201. https://doi.org/10.1103/PhysRevMaterials.9.015201.
[31] A. R. Abe, R. H. Crabtree, G. H. Brudvig, *Chem. Soc. Rev.* **2013**, *42*, 2247–2252. https://doi.org/10.1039/C2CS35225G.
[32] C. E. Frey, P. Kurz, *Chem. - Eur. J.* **2015**, *21*, 14958–14968. https://doi.org/10.1002/chem.201501367.
[33] R. Auguste, H. L. Chan, E. Romanovskaia, J. Qiu, R. Schoell, M. Liedke, M. Butterling, E. Hirschmann, A. Attallah, A. Wagner, *npj Mater. Degradation* **2022**, *6*, 61. https://doi.org/10.1038/s41529-022-00269-7.
[34] A. Bergmann, E. Martinez-Moreno, D. Teschner, P. Chernev, M. Gliech, J. F. de Araújo, T. Reier, H. Dau, P. Strasser, *Nat. Commun.* **2015**, *6*, 8625. https://doi.org/10.1038/ncomms9625.
[35] M. F. Zscherp, M. Bastianello, S. Nappini, E. Magnano, D. Badocco, S. Gross, M. T. Elm, *J. Mater. Chem. C* **2022**, *10*, 2976–2987. https://doi.org/10.1039/D1TC05871A.
[36] G. Jonker, *J. Phys. Chem. Solids* **1959**, *9*, 165–175. https://doi.org/10.1016/0022-3697(59)90206-9.
[37] E. Hirschmann, M. Butterling, U. H. Acosta, M. Liedke, A. Attallah, P. Petring, M. Görler, R. Krause-Rehberg, A. Wagner, *J. Instrument.* **2021**, *16*, P08001. https://doi.org/10.1088/1748-0221/16/08/P08001.
[38] R. Krause-Rehberg, H. S. Leipner, *Positron Annihilation in Semiconductors, Vol. 127 in Solid-State Sciences*, Springer, Berlin **1999**.
[39] Z. Ma, P. Monalisha, Z. Tan, E. Pellicer, M. O. Liedke, M. Butterling, A. G. Attallah, E. Hirschmann, A. Wagner, F. Ibrahim, *J. Materiom.* **2024**, *10*, 870–879. https://doi.org/10.1016/j.jmat.2023.10.007.
[40] J. V. Olsen, P. Kirkegaard, N. J. Pedersen, M. Eldrup, *Phys. Status Solidi C* **2007**, *4*, 4004–4006. https://doi.org/10.1002/pssc.200675868.
[41] L. A. Bromley, *AIChE J.* **1973**, *19*, 313–320. https://doi.org/10.1002/aic.690190216.

Manuscript received: August 15, 2025
Revised manuscript received: October 27, 2025
Accepted manuscript online: November 7, 2025
Version of record online: ■■, ■■